Electronic Supplementary Information (ESI)

Constructing asymmetric dual active sites through symbiotic effect for achieving efficient and selective photoreduction of CO_2 to C_2H_4

Yong Xu,[#a] Ping Wang,[#a] Man Zhang,[a] Weili Dai,*[a] Yuxuan Xu,[a] Jian-Ping Zou[a] and Xubiao Luo[ab]

[a]*Key Laboratory of Jiangxi Province for Persistent Pollutants Prevention Control and Resource Reuse, Nanchang Hangkong University, Nanchang 330063, P. K. China.*

[b] *School of Life Science, Jinggangshan University, Ji'an 343009, P. R. China*

*Corresponding Author
E-mail: wldai81@126.com

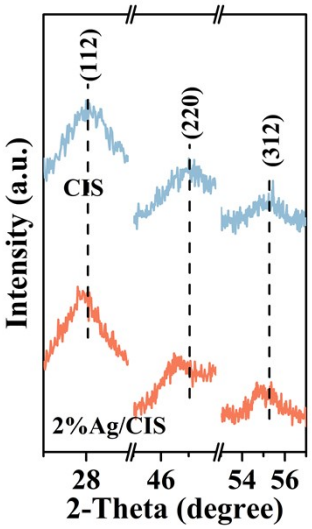

Fig. S1. Localized magnified XRD diffraction patterns of CIS and 2%Ag/CIS.

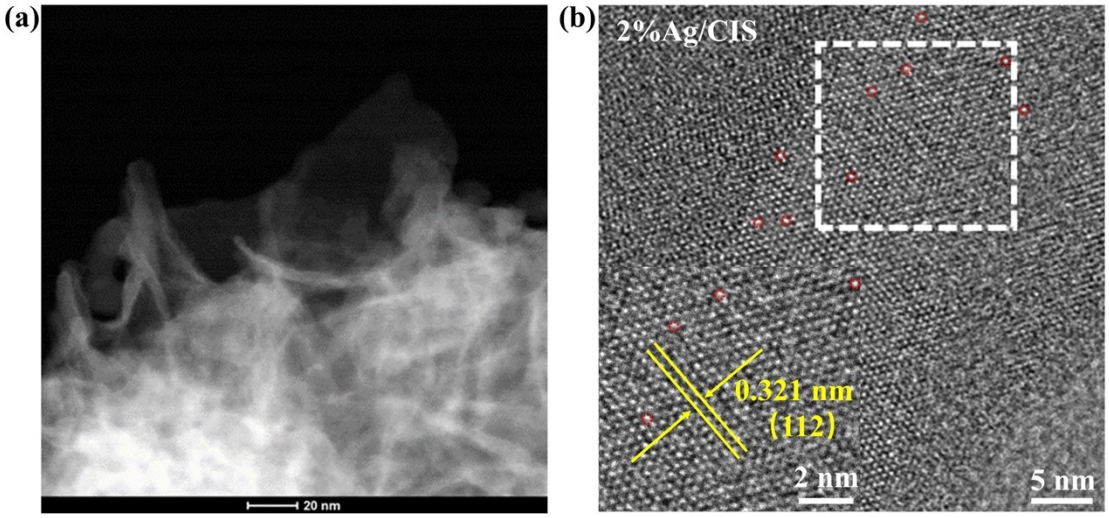

Fig. S2. TEM (a) and HRTEM (b) images of 2%Ag/CIS.

After heteroatom Ag substituting Cu atom, the binding ability of Ag and S is weaker than Cu and S due to poor ability of electron donating (Ag 0.30 e, Cu 0.42 e) (Fig. S11). Therefore, electron nonequilibrium and lattice mismatch are formed with Ag confinement. The adjacent S atom escapes from the lattice to produce S_v. The

coordination numbers of Ag and Cu as well as In atoms around S_v decrease. The S atom is tightly pulled by other metal atoms, causing a longer Ag-S bond length (2.40 Å, Table S1) than the normal Cu-S bond length (2.334 Å) in $CuInS_2$. Ag-S enlargement leads to lattice and interlayer broadening. Meanwhile, Cu-S bond lengths (2.334 Å) around the S_v area emerge distorted to accomplish thermodynamic stability. Atomic arrangement variation brings about huge morphological changes. And thus $CuInS_2$ transforms from nanoparticles to nanosheets.

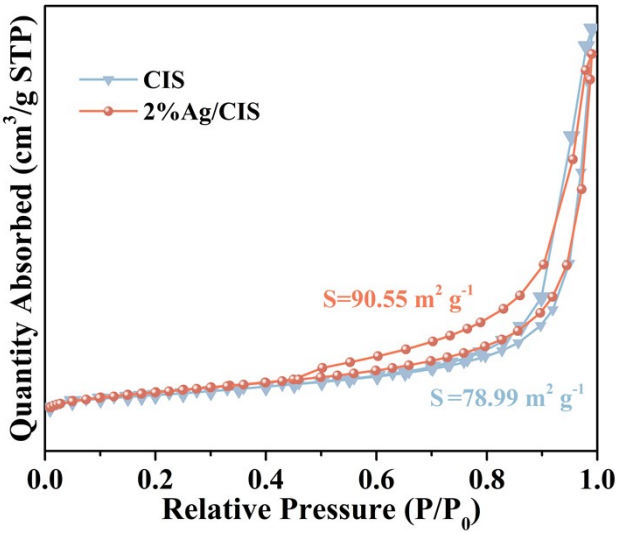

Fig. S3. N_2 adsorption–desorption isotherm diagrams of CIS and 2%Ag/CIS.

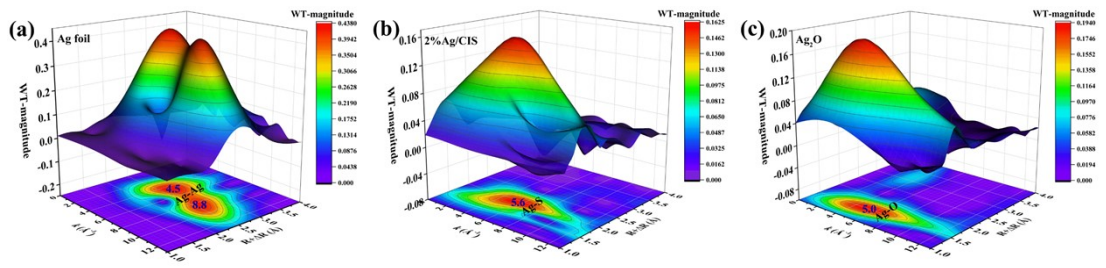

Fig. S4. The WT of (a) Ag foil, (b) 2%Ag/CIS and (c) Ag_2O.

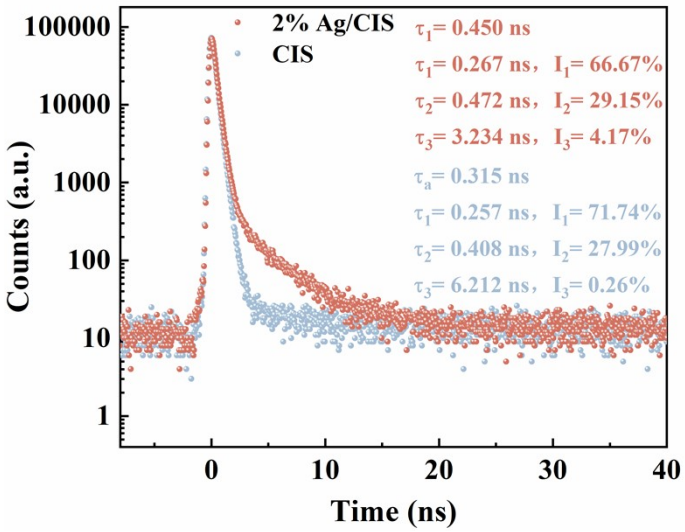

Fig. S5. Results of positron annihilation experiments.

The corresponding intensity obtained from the positron annihilation lifetime spectrum can be used to infer the degree of defect. The lifetime of positrons trapped in these defects will be longer than their lifetime in non-defective crystals. As shown in Fig. S5, the short lifetime of τ_1 represents the annihilation life of non-defective materials, while long lifetime τ_2 represents the lifetime of positrons in the captured state. The τ_3 attributes to the annihilation of positrons formed in the intergranular region characterized by large volume. According to formula $C_d = \frac{I_2}{\mu I_1}\left(\frac{1}{\tau_b} - \frac{1}{\tau_2}\right)$ $\left(\frac{1}{\tau_b} = \frac{I_1}{\tau_{1+}} \frac{I_2}{\tau_2}\right)$, the relative strength of I_2 generally reflects the degree of defect concentration.

Therefore, whether analyzed from the lifetime (τ_a or τ_2) or I_2 strength, the defect concentration of 2%Ag/CIS is much higher than that of pure CIS. Combined with the EPR test results, it is sufficient to confirm that the content of S_v in 2%Ag/CIS is high.

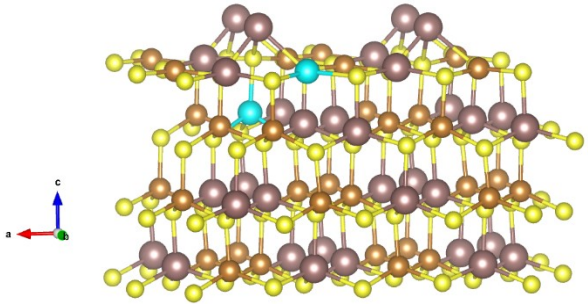

Fig. S6. The model of Ag/CIS(without S_v).

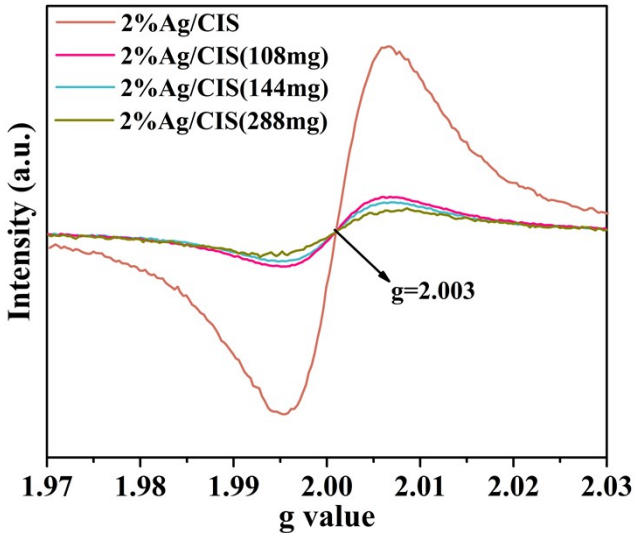

Fig. S7. ESR spectra. During the 2%Ag/CIS preparation process, the amount of TAA increased from 72 mg to 108, 144 and 288 mg, while other conditions remained unchanged.

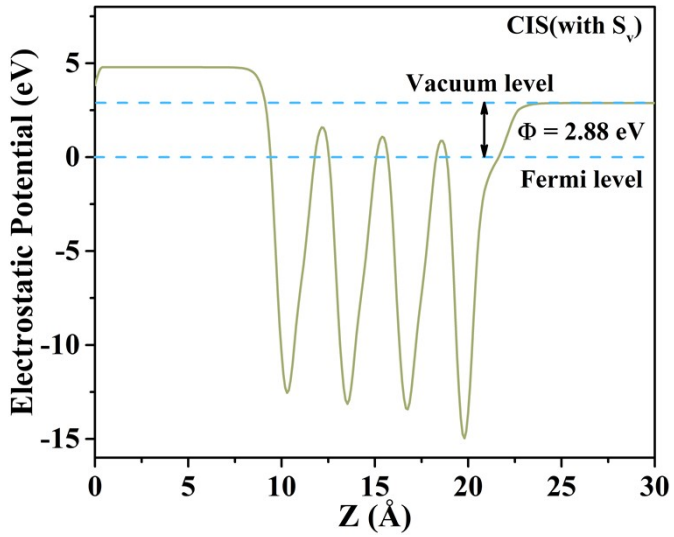

Fig. S8. The calculated electrostatic potentials of CIS(with S_v).

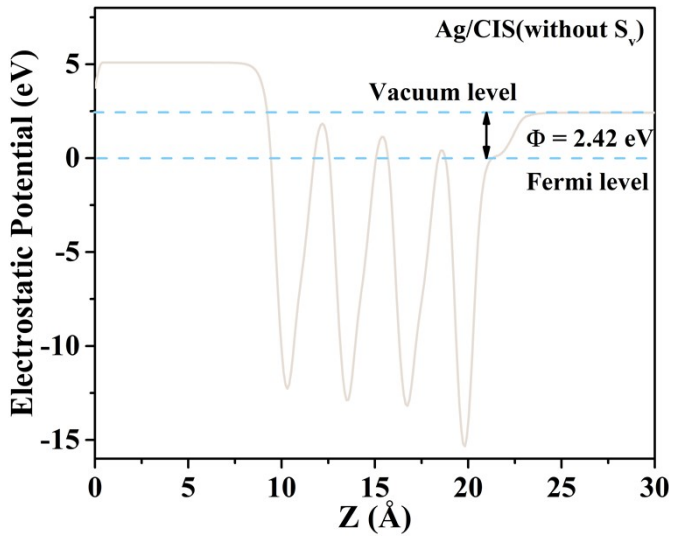

Fig. S9. The calculated electrostatic potentials of Ag/CIS(without S_v).

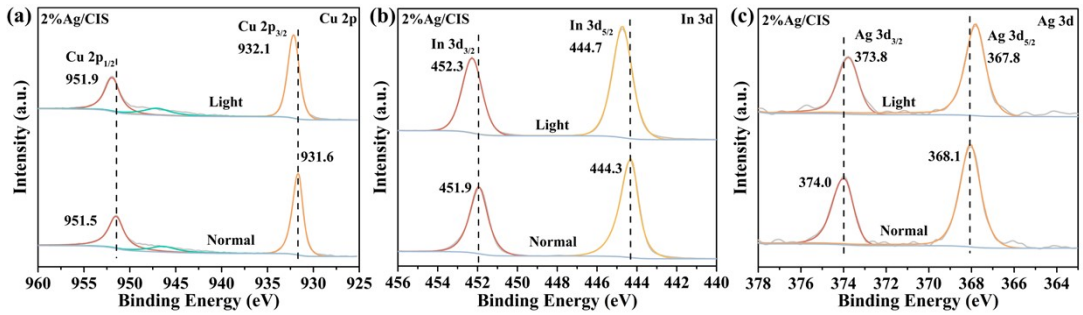

Fig. S10. In situ XPS spectra of (a) Cu 2p, (b) In 3d and (c) Ag 3d.

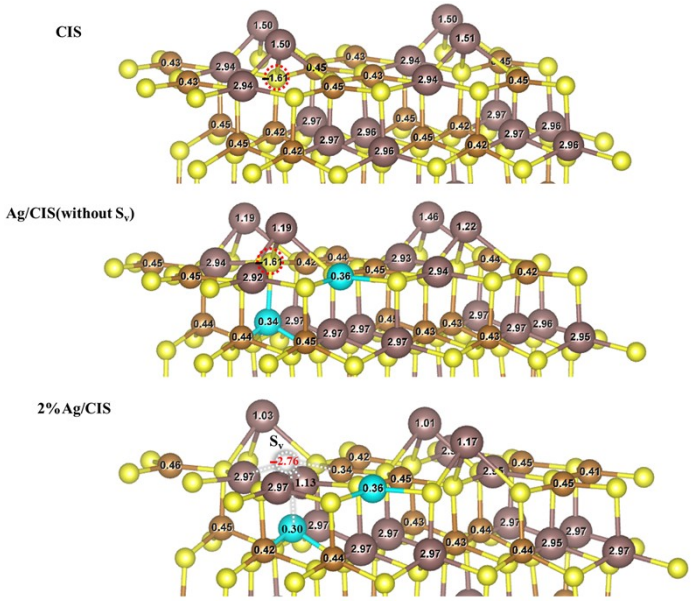

Fig. S11. Differential charge maps of CIS, Ag/CIS(without S_V) and 2%Ag/CIS. Positive values represent the number of electrons lost, while negative values represent the number of electrons obtained.

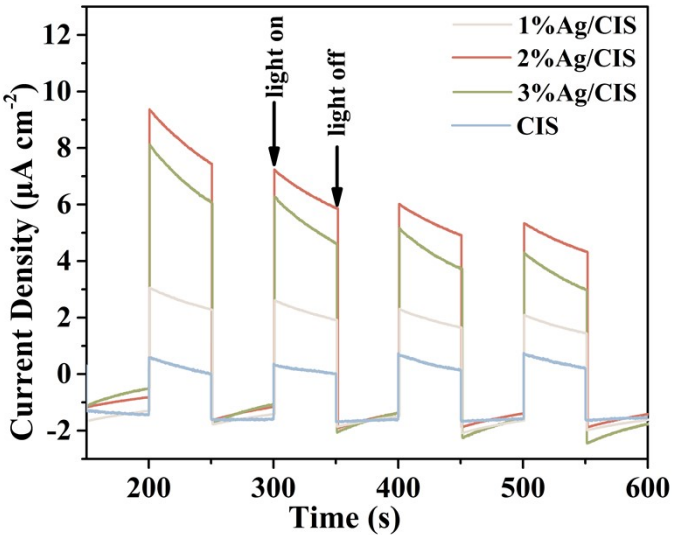

Fig. S12. Transient photocurrent response.

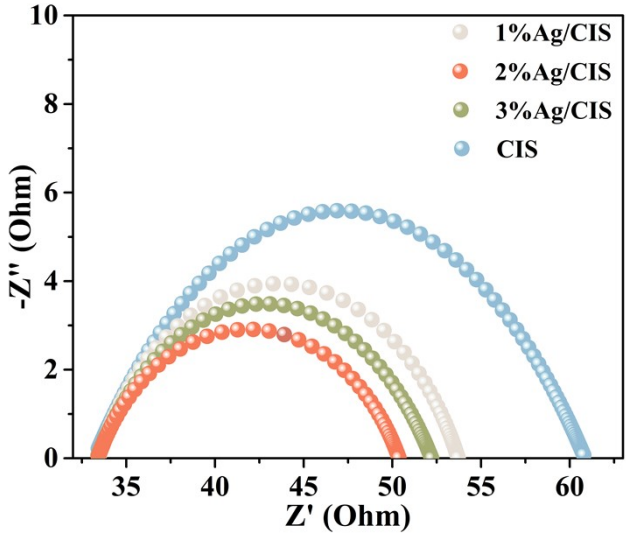

Fig. S13. EIS Nyquist plots.

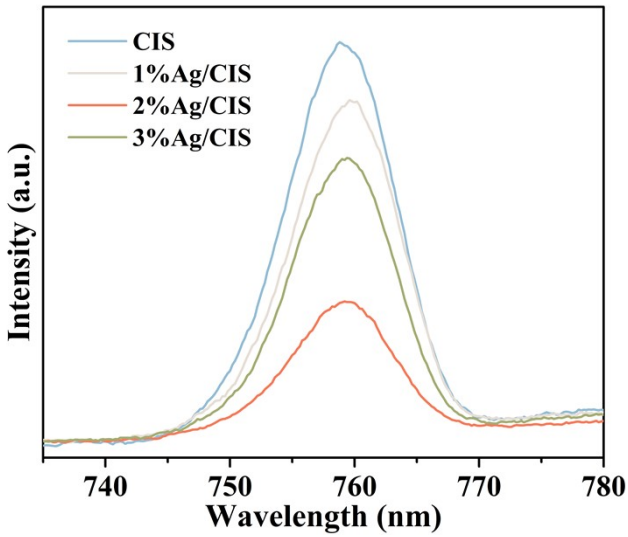

Fig. S14. Steady-state PL spectra.

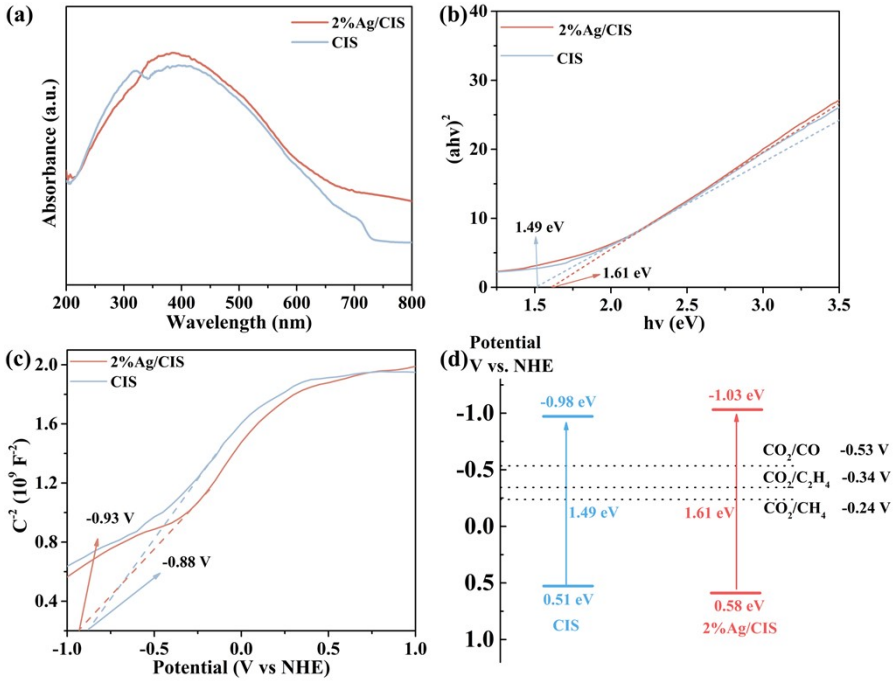

Fig. S15. (a) UV-vis diffuse reflectance spectra (DRS), (b) obtained bandgaps of 1.49 eV and 1.61 eV, estimated by plotting $(\alpha h\nu)^2$ versus hν (Tauc plot). α and ν are the absorbance and wavenumber. (c) Mott–Schottky plots. (d) Electronic band structure alignments. According to the Mott-Schottky plots, the flat band potentials of CIS and

2%Ag/CIS are -0.88 V and -0.93 V, respectively. Usually, the conduction band potential of n-type semiconductors is about 0.1 V lower than that of flat band.[1] Therefore, the minimum conduction band values (CB) of CIS and 2%Ag/CIS are -0.98 V and -1.03 V, respectively.

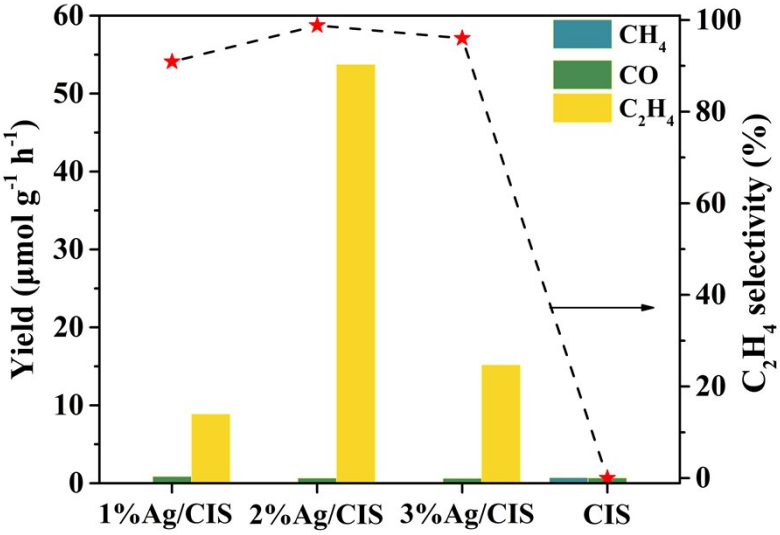

Fig. S16. Comparison of photoreduction product yield and ethylene selectivity.

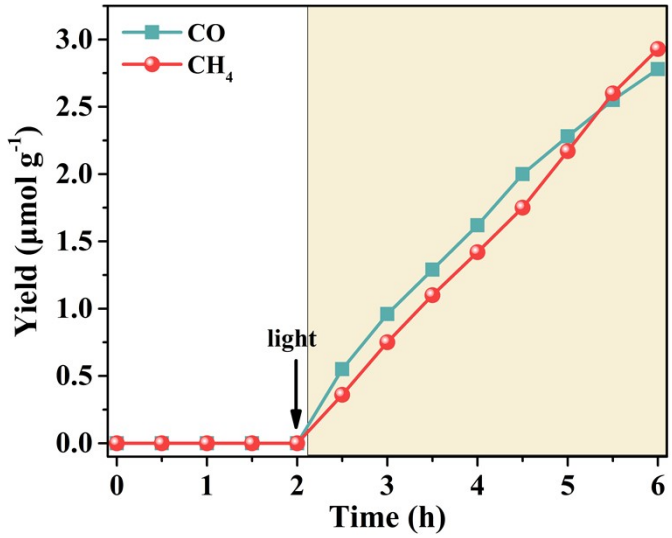

Fig. S17. Products of photocatalytic CO_2 reduction for CIS.

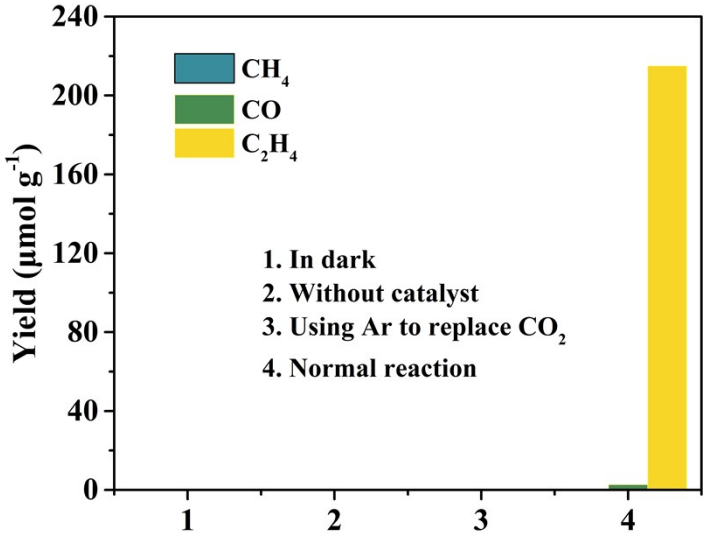

Fig. S18. Control experiments for 2%Ag/CIS.

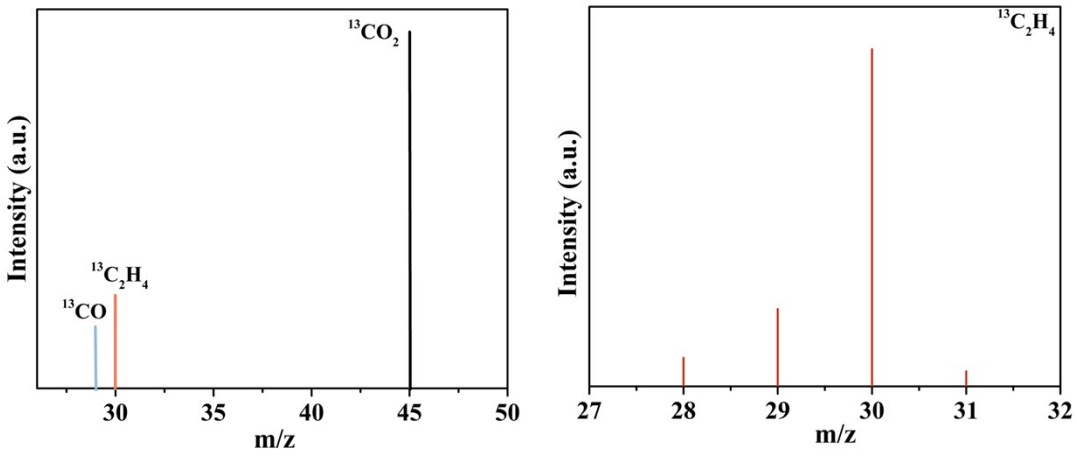

Fig. S19. The mass spectra analysis of products over 2%Ag/CIS with $^{13}CO_2$ as feedstock.

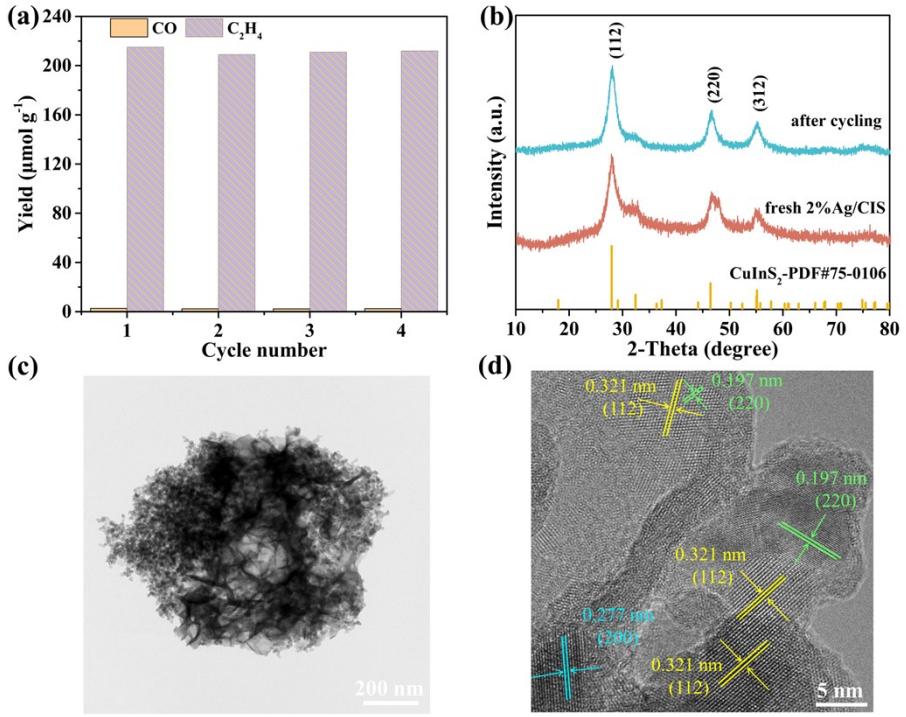

Fig. S20. (a) Cyclic experiment of 2%Ag/CIS. (b) Comparison of XRD before and after cyclic experiment. (c, d) TEM and HRTEM images after cyclic experiment.

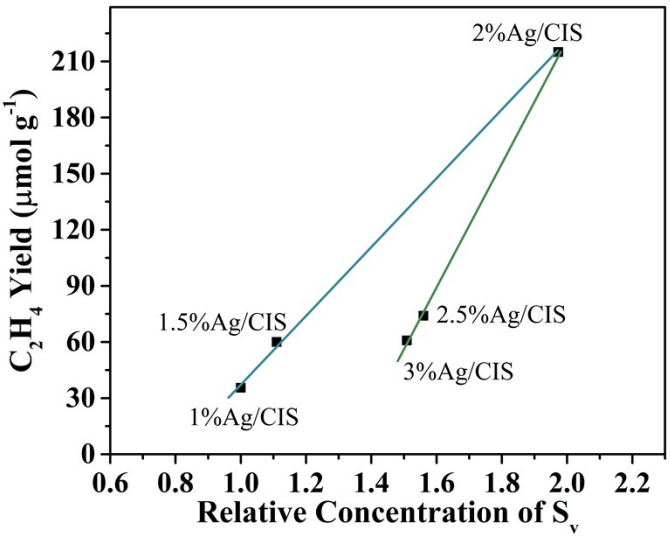

Fig. S21. The relationship between S_v concentration and C_2H_4 yield.

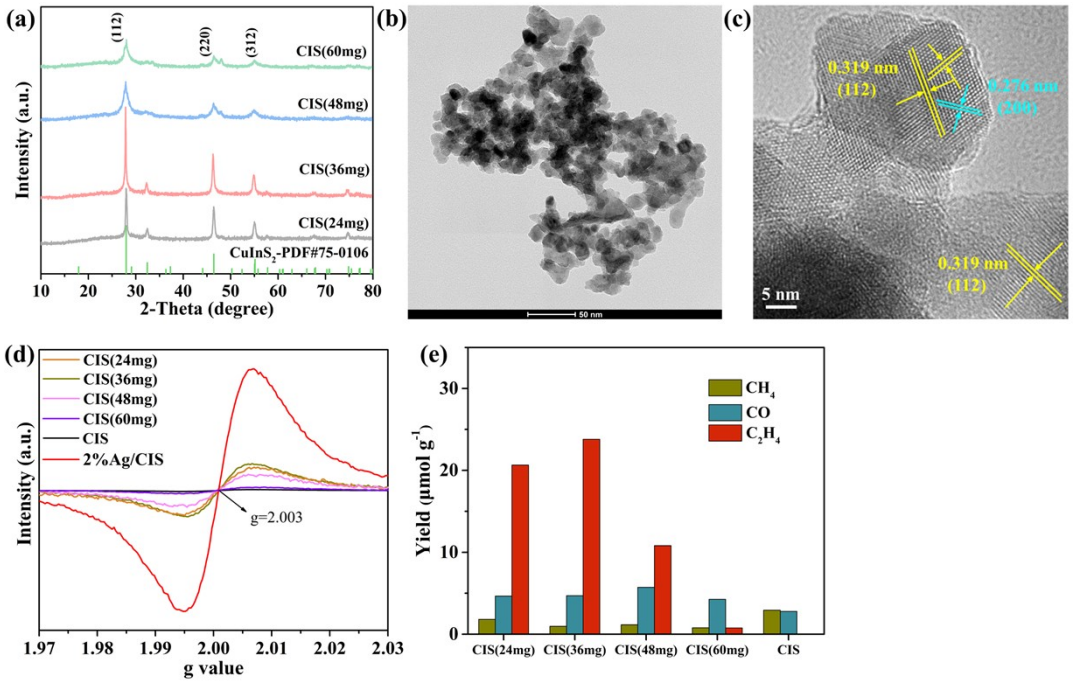

Fig. S22. (a) Pure phase $CuInS_2$ materials prepared by reducing TAA dosages, (b, c) corresponding TEM images, (d) ESR spectra, (e) comparison of catalytic performance.

Without adding $AgNO_3$ and keeping other preparation conditions unchanged, the dosage of TAA was reduced from 72 mg to 60, 48, 36, and 24 mg, and the resulting

materials are labeled as CIS(60mg), CIS(48mg), CIS(36mg) and CIS(24mg), respectively. The XRD patterns of the prepared materials are shown in Fig. S23a below. It can be seen that although the materials obtained with a decrease in TAA dosage are all pure phase $CuInS_2$, the quality of obtained materials decreases with a decrease in TAA dosage. The narrowing of the half peak width of the (112) crystal plane in CIS(36mg) material may be caused by the enlargement of the nanoparticles. From TEM images (Fig. S23bc) of CIS(36mg), it can be seen that the morphology is consistent with CIS as nanoparticles, without the formation of sheet-like structure or change in lattice width. Additionally, ESR testing shows that the S_v intensity of CIS(36mg) is the highest but much lower than that of 2%Ag/CIS (Fig. S23d). This result indicates that the presence of Ag-S_v-In structure is beneficial for stabilizing high concentration S_v. The performance comparison results of above materials are shown in Fig. S23e, when the TAA dosage is reduced to 60 mg, CIS(60mg) acts as a catalyst for photocatalytic reduction of CO_2 to produce a small amount of C_2H_4 (0.76 μmol g^{-1}). When the TAA dosage is reduced to 36 mg, the prepared CIS(36 mg) catalyzes CO_2 reduction to produce C_2H_4 at a rate of 23.8 μmol g^{-1}, which is much lower than the catalytic capacity of 2%Ag/CIS (215 μmol g^{-1}). The performance comparison results confirm the stability of Ag-S_v-In structure and the important role of S_v in catalysis.

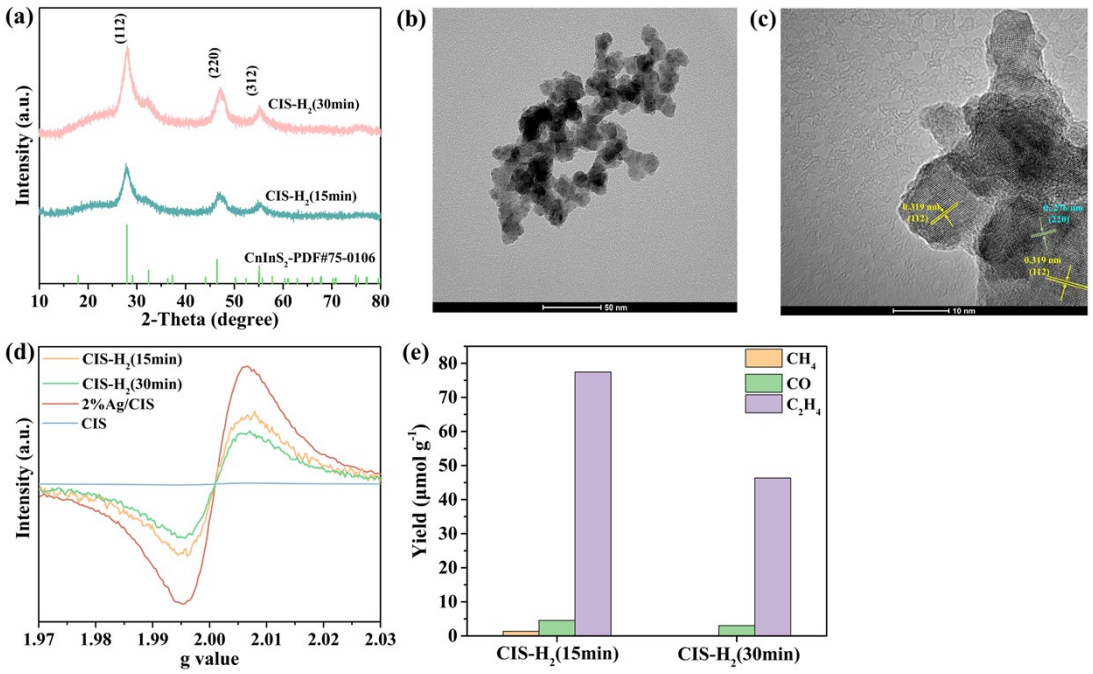

Fig. S23. (a) Prepared $CuInS_2$ materials with H_2 reduction, (b, c) corresponding TEM images, (d) ESR spectra, (e) comparison of catalytic performance.

$CuInS_2$ nanoparticles (50 mg) were heated at 180 ℃ in a 5%H_2/Ar atmosphere for 15 and 30 min, the obtained materials are marked as CIS-H_2(15min) and CIS-H_2(30min) respectively. The XRD patterns of the prepared materials are shown in Fig. S24a below, CIS-H_2(15min) and CIS-H_2(30min) are all pure phase $CuInS_2$. The materials obtained from H_2 reduction of CIS are still nanoparticles (Fig. S24b), without the formation of sheet-like structure or change in lattice width (Fig. S24c). In ESR testing (Fig. S24d), the S_v concentrations of CIS-H_2 materials are higher than that of CIS(36mg), but significantly lower than that of 2%Ag/CIS, which further confirms that the presence of Ag-S_v-In structure is beneficial for stabilizing high concentration S_v. And the performance comparison results are shown in Fig. S24e, when CIS-H_2(15min) is used as a photocatalyst, the rate of C_2H_4 production is 77 μmol g^{-1}, which is much lower than the catalytic capacity of 2%Ag/CIS (215 μmol g^{-1}). This result further proves

that it is possible to obtain C_2H_4 as long as there are dual sites of S_v and In, and also proves that Ag-S_v-In can stabilize high concentration S_v.

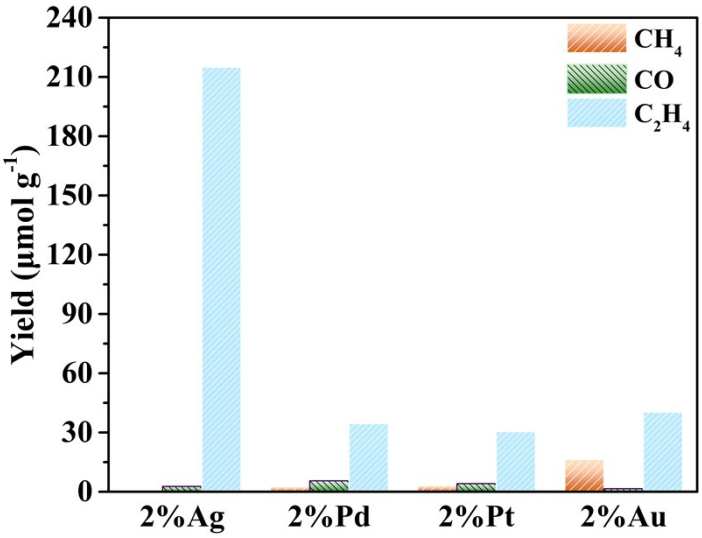

Fig. S24. Comparison of photocatalytic performance with other metal-doped CIS.

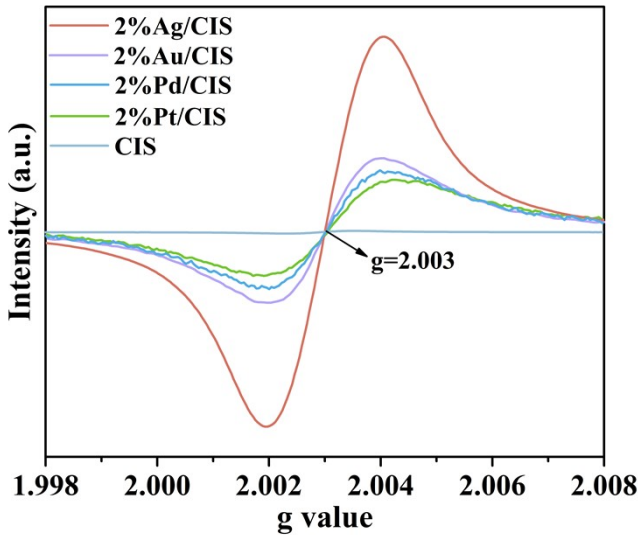

Fig. S25. Comparison of ESR signals of CIS doped with different metals.

The valence state of Cu in $CuInS_2$ material is +1, and the doping atom tended to substitute an atom with the same approximate valence state. Therefore, Ag is likely to replace Cu atom. On the other hand, the solubility product constant of Ag_2S (K_{sp}= $6.3x10^{-50}$) is smaller than that of Cu_2S (K_{sp}= $2.5x10^{-48}$) and CuS (K_{sp}= $1.3x10^{-36}$), making it easier for Ag to bond with S. However, precious metals of Au, Pd, and Pt have weak bonding with S, as a result, the concentration of S_v formed is relatively small. And as displayed in Fig. S21, a large amount of S_v is generated after Ag doping, while the concentration of S_v formed after noble metal Au, Pd, and Pt doping is much lower. Due to the important role of S_v in the adsorption and activation of CO_2 molecules, so Ag doped CIS has the highest activity. In addition, Ag doping triggers the symbiotic effect to promote the formation of S_v, while the presence of Ag-S_v-In structure can promote the stable existence of high concentration S_v. And the photogenerated electrons captured by Ag single atoms can be selectively transferred to S_v, which is beneficial for the adsorption, activation, and hydrogenation reduction reactions of CO_2 molecules.

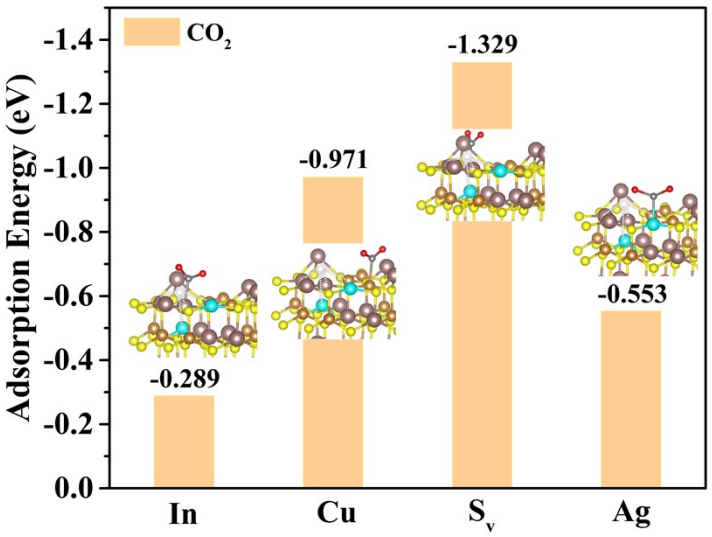

Fig. S26. Calculated CO_2 adsorption energies and corresponding structures.

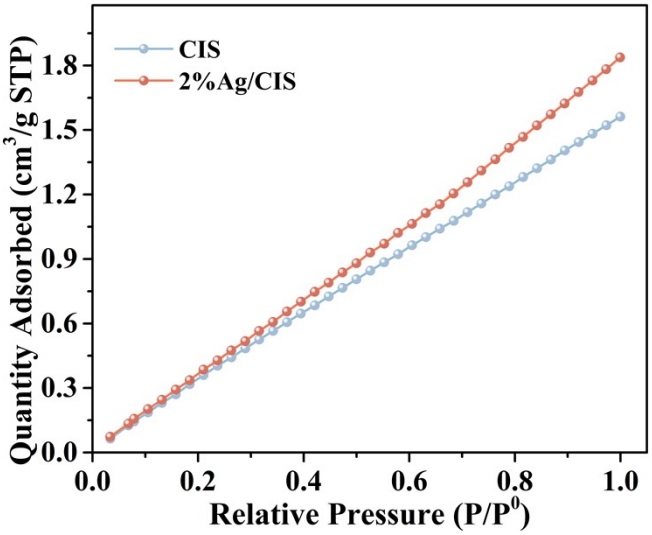

Fig. S27. The adsorption curves of CO_2 with CIS and 2%Ag/CIS.

Table S1. EXAFS fitting parameters at the Ag K-edge for various samples (S_o^2=0.722).

Sample	Shell	CN[a]	R(Å)[b]	σ^2(Å^2)[c]	ΔE_0(eV)[d]	R factor
Ag foil	Ag-Ag	12*	2.860±0.001	0.0094±0.0002	1.2±0.3	0.0031
Sample Ag	Ag-S	2.8±0.5	2.396±0.014	0.0093±0.0026	-4.3±3.1	0.0197

[a]*CN*, coordination number; [b]*R*, the distance to the neighboring atom; [c]σ^2, the Mean Square Relative Displacement (MSRD); [d]ΔE_0, inner potential correction; *R* factor indicates the goodness of the fit. S_0^2 was fixed to 0.722, according to the experimental EXAFS fit of Ag foil by fixing *CN* as the known crystallographic value. * This value was fixed during EXAFS fitting, based on the known structure of Ag. Fitting range: 3.0 ≤ *k* (/Å) ≤ 14.1 and 1.0 ≤ *R* (Å) ≤ 3.3 (Ag foil); 2.0 ≤ *k* (/Å) ≤ 10.0 and 1.0 ≤ *R* (Å) ≤ 3.0 (Sample Ag). A reasonable range of EXAFS fitting parameters: 0.700 < S_0^2 < 1.000; *CN* > 0; σ^2 > 0 Å^2; $|\Delta E_0|$ < 10 eV; *R* factor < 0.02.

Table S2. The content of various elements in 2%Ag/CIS photocatalyst measured by ICP-OES.

Element	Mass Fraction (wt%)	Molar ratio
Ag	0.98	0.02
Cu	25.75	1.00
In	47.34	1.02
S	25.93	2.00

The atomic fraction of Ag is calculated using the molar amount of Ag compared to the total molar amount of Ag and Cu. The molar ratio of Ag to Cu is 0.02:1, so the atomic fraction of Ag is $0.02/(0.02+1)\times 100\%$, which is nearly 2%. Therefore, the obtained material is labeled as 2%Ag/CIS.

Table S3. Comparison of the reaction conditions and performances with other catalysts for photocatalytic CO_2 reduction to C_2H_4.

	Catalyst	Light source	Reaction condition	Products and activity ($\mu mol\ g^{-1}\ h^{-1}$)	Seletivity of C_2H_4	Mass of catalysts	References
1	2%Ag/CIS	300 W Xe lamp with an AM 1.5G filter	Gas-solid, H_2O	C_2H_4: 53.74; CO: 0.68	98.8%	5 mg	This work
2	CuACS/PCN	high-pressure 300 W Xe lamp	Gas-solution, H_2O, $[Ru(bpy)_3]^{2+}$, TEOA	C_2H_4: 10.17; CH_4: 8.95	53.2%	5 mg	Ref. 2
3	BPQDs-WO_3	300 W Xe lamp	Gas-solid, H_2O	C_2H_4: 11.0; CO: 72.47	13.2%	10 mg	Ref. 3
4	$Cu_{0.01}$/3DOM-TiO_2	Xe lamp (200 mW/cm^2, 320-780 nm)	Gas-solution, H_2O	C_2H_4: 6.99; CH_4: 3.45; CO: 1.50	58.4%	5 mg	Ref. 4
5	$Cu^{\delta+}/CeO_2$-TiO_2	Xe lamp (200 mW/cm^2, 320-850 nm)	Gas-solution, H_2O	C_2H_4: 4.51; CH_4: 1.52; CO: 3.47	47.5%	10 mg	Ref. 5
6	S_v-CdS@ZIF-8	300 W Xe lamp with a 420 nm cut-off filter	Gas-solid, H_2O	C_2H_4: 0.8; CO: 5.83	12.8%	20 mg	Ref. 6
7	$CuGaS_2$	450 W Xe lamp (with UV cut-off filter (KG-2 filter and CGA-400) filter)	Gas-solution, H_2O, pH=12 (0.1M NaOH)	C_2H_4: 20.6; CH_4: 1.88; CO: 6.25; H_2: 1.25	75.1%	5 mg	Ref. 7
8	MIL-88B-NS40	300 W Xe lamp with a 420 nm cut-off filter (200 mW/cm^2)	Gas-solid, H_2O	C_2H_4: 17.7; CH_4: 51.23; CO: 673.41	10.6%	5 mg	Ref. 8
9	CGS/GS	300 W Xe lamp with a 420 nm cut-off filter (λ > 420 nm)	Gas-solid, H_2O	C_2H_4: 18.0; CH_4: 12.42; CO: 43.79	24.3 %	20 mg	Ref. 9
10	CuO_X@p-ZnO	300 W Xe lamp (100 mW/cm^2, 320-780 nm)	Gas-solid, H_2O	C_2H_4: 2.7; CH_4: 2.2; CO: 3.3	32.9%	5 mg	Ref. 10
11	Mo-COF	300 W Xe lamp ($\lambda \geq 420$ nm)	Gas-solid, H_2O	C_2H_4: 3.57; CH_4: 1.08; CO: 6.19	42.9%	10 mg	Ref. 11

12	V_s-$NiCo_2S_4$-NF	300 W Xe lamp (150 mW/cm^2)	Gas-solid, H_2O	C_2H_4: 13.42; CH_4: 1.52; CO: 8.57	57.1 %	20 mg	Ref. 12
13	In-T/CN	UV LED ((λ = 365 nm)	Gas-solid, H_2O	C_2H_4: 1.41; CH_4: 7.31; CO: 2.32	12.8%	50 mg	Ref. 13
14	$CsPbBr_3$	300 W Xe lamp with an AM 1.5G filter	Gas-solution, ethyl acetate, H_2O	C_2H_4: 9.3; C_3H_8: 2.26; C_2H_6: 3.42; CH_4: 3.78; H_2: 8.48	34.1%	/	Ref. 14
15	CCN-W	300 W Xe lamp (full spectrum light Irradiation)	Gas-solution, $NaHCO_3$ powder, H_2SO_4 (2 M, 0.3 mL)	C_2H_4: 1.71; CH_4: 4.45; CO: 5.75	14.4%	5 mg	Ref. 15
16	α-Fe_2O_3/GR/Bi_2O_2S	300 W Xe lamp with a 420 nm cut-off filter (100 mW/cm^2)	Gas-solid, H_2O	C_2H_4: 2.88; CH_4: 4.27; CO: 13.00	14.3%	50 mg	Ref. 16
17	Mildly oxidized $FeCoS_2$	300 W Xe lamp with an AM 1.5G filter (100 mW/cm^2)	Gas-solid, H_2O	C_2H_4: 20.1; CO: 4.13	82.9%	10 mg	Ref. 17
18	Bi_2S_3@In_2S_3	Xe lamp of different wavelengths	Gas-solid, H_2O	C_2H_4: 11.81; CO: 1.98	86.0%	5 mg	Ref. 18
19	TCPP/Cu_2O/LDH-70	300 W Xe lamp (100 mW/cm^2)	Gas-solution, H_2O	C_2H_4: 1.56; C_2H_6: 1.92; CH_4: 3.01; CO: 26.18	4.8%	50 mg	Ref. 19
20	0.15-Cu_2O@Cu-CN	300 W Xe lamp with a 420 nm cut-off filter	Gas-solution, H_2O, TEOA	C_2H_4: 46.27; CH_4: 7.25 CO: 61.15 H_2: 2.75	40.3%	50 mg	Ref. 20
21	Cu_1/TiO_2	Xe lamp (full spectrum)	Gas-solution,H_2O, TEOA	C_2H_4: 60.4; CH_4: 17.86 CO: 31.24	75.2%	20 mg	Ref. 21
22	3.6-$Cu_1/W_{18}O_{49}$	300 W Xe lamp (453 mW/cm^2)	Gas-solid, H_2O	C_2H_4: 4.9; CH_4: 2.2 CO: 5.1	72.8%	5 mg	Ref. 22
23	CCS-H1	300 W Xe lamp with a 420 nm cut-off filter	Gas-solution,H_2O	C_2H_4: 30.02; CO: 8.74	77.5%	20 mg	Ref. 23

24	$CuO@Cu_2V_2O_7$	300 W Xe lamp	Gas-solution,H_2O, TEOA	C_2H_4: 29.57; CH_4: 3.81 CO: 118.0	19.5%	50 mg	Ref. 24

References

1 G. Wang, Z. Chen, T. Wang, D. Wang and J. Mao, *Angew. Chem. Int. Ed.*, 2022, **61**, e202210789.

2 W. Xie, K. Li, X. H. Liu, X. Zhang and H. Huang, *Adv. Mater.*, 2022, **35**, 2208132.

3 W. Gao, X. Bai, Y. Gao, J. Liu, H. He, Y. Yang, Q. Han, X. Wang, X. Wu, J. Wang, F. Fan, Y. Zhou, C. Li and Z. Zou, *Chem. Commun.*, 2020, **56**, 7777−7780.

4 C. Chen, T. Wang, K. Yan, S. Liu, Y. Zhao and B. Li, *Inorg. Chem. Front.*, 2022, **9**, 4753-4767.

5 T. Wang, L. Chen, C. Chen, M. Huang, Y. Huang, S. Liu and B. Li, *ACS Nano*, 2022, **16**, 2306−2318.

6 F. Tian, H. Zhang, S. Liu, T. Wu, J. Yu, D. Wang, X. Jin and C. Peng, *Appl. Catal. B: Environ.*, 2021, **285**, 119834.

7 S. Chakraborty, R. Das, M. Riyaz, K. Das, A. K. Singh, D. Bagchi, C. P. Vinod and S. C. Peter, *Angew. Chem. Int. Ed.*, 2022, **62**, e202216613.

8 F. Guo, R. X. Li, S. Yang, X. Y. Zhang, H. Yu, J. J. Urban and W. Y. Sun, *Angew. Chem. Int. Ed.*, 2023, **62**, e202216232.

9 J. Wang, C. Yang, L. Mao, X. Cai, Z. Geng, H. Zhang, J. Zhang, X. Tan, J. Ye and T. Yu, *Adv. Funct. Mater.*, 2023, **33**, 2213901.

10 W. Wang, C. Deng, S. Xie, Y. Li, W. Zhang, H. Sheng, C. Chen and J. Zhao, *J. Am. Chem. Soc.*, 2021, **143**, 2984−2993.

11 M. Kou, W. Liu, Y. Wang, J. Huang, Y. Chen, Y. Zhou, Y. Chen, M. Ma, K. Lei, H. Xie, P. K. Wong and L. Ye, *Appl. Catal. B: Environ.*, 2021, **291**, 120146.

12 X. Luo, L. Qiao, S. Zhang, Q. Li, Y. Liao, S. Rao, H. Liu and Y. Zhao, *Appl. Surf. Sci.*, 2022, **601**, 154184.

13 J. Park, H. Liu, G. Piao, U. Kang, H. W. Jeong, C. Janáky and H. Park, *Chem. Eng. J.*, 2022, **437**, 135388.

14 B. N. Choi, J. Y. Seo, Z. An, P. J. Yoo and C. H. Chung, *Chem. Eng. J.*, 2022, **430,** 132807.

15 Y. Liang, X. Wu, X. Liu, C. Li and S. Liu, *Appl. Catal. B: Environ.*, 2022, **304**, 120978.

16 Y. Luo, H. Han, G. Zhang, Q. Wang and Y. jia, *Sep. Purif. Technol.*, 2023, **314**, 123607.

17 Y. Wu, Q. Chen, J. Zhu, K. Zheng, M. Wu, M. Fan, W. Yan, J. Hu, J. Zhu, Y. Pan, X. Jiao, Y. Sun and Y. Xie, *Angew. Chem. Int. Ed.*, 2023, **62**, e202301075.

18 K. Yan, D. Wu, T. Wang, C. Chen, S. Liu, Y. Hu, C. Gao, H. Chen and B. Li, *ACS Catal.*, 2023, **13**, 2302−2312.

19 C. Xia, R. T. Guo, Z. X. Bi, Z. R. Zhang, C. F. Li and W. G. Pan, *Dalton Trans.*, 2023, **52**, 12742−12754.

20 S. Qiao, Y. Chen, Y. Tang, J. Yuan, J. Shen, D. Zhang, Y. Du, Z. Li, D. Yuan, H. Tang and C. Liu, *Chem. Eng. J.*, 2023, **454**, 140321.

21 Q. Wang, Y. Zhang, M. Lin, H. Wang, Y. Bai, C. Liu, J. Lu, Q. Luo, G. Wang, H. L. Jiang, T. Yao and X. Zheng, *Adv. Energy. Mater.*, 2023, **13**, 2302692.

22 Y. Mao, M. Zhang, G. Zhai, S. Si, D. Liu, K. Song, Y. Liu, Z. Wang, Z. Zheng, P. Wang, Y. Dai, H. Cheng and B. Huang, *Adv. Sci.*, 2024, doi: 10.1002/advs.202401933.

23 Y. Nie, Y. Li, C. An, X. Tan, Z. Hu, J. Ye and T. Yu, *Appl. Catal. B: Environ.*, 2024, **345**, 123704.

24 X. Li, F. Li, S. Tong, Y. Cao, Y. Jiang, Z. Wang, W. Lu, J. Wu, T. Zhou, J. Lin and Y. Liu, *J Alloy Compd.*, 2024, **984**, 173986.